Bioactive Materials 30 (2023) 142–153

Contents lists available at ScienceDirect

Bioactive Materials

journal homepage: www.keaipublishing.com/en/journals/bioactive-materials

Micromolded honeycomb scaffold design to support the generation of a bilayered RPE and photoreceptor cell construct

In-Kyu Lee [a,b,1], Ruosen Xie [b,c,d,e,1], Agustin Luz-Madrigal [e,f,g,1], Seunghwan Min [a,b,1], Jingcheng Zhu [b,d], Jiahe Jin [f], Kimberly L. Edwards [f], M. Joseph Phillips [f], Allison L. Ludwig [e], David M. Gamm [c,e,f,g,**], Shaoqin Gong [b,c,d,e,*], Zhenqiang Ma [a,h,i,j,***]

[a] Department of Electrical and Computer Engineering, University of Wisconsin-Madison, Madison, WI, 53706, USA
[b] Wisconsin Institute for Discovery, University of Wisconsin-Madison, Madison, WI, 53715, USA
[c] Department of Ophthalmology and Visual Sciences, University of Wisconsin-Madison, Madison, WI, 53705, USA
[d] Department of Biomedical Engineering, University of Wisconsin-Madison, Madison, WI, 53706, USA
[e] McPherson Eye Research Institute, University of Wisconsin-Madison, Madison, WI, 53705, USA
[f] Waisman Center, University of Wisconsin-Madison, Madison, WI, 53705, USA
[g] Department of Comparative Biomedical Sciences, University of Wisconsin–Madison, Madison, WI, 53706, USA
[h] Department of Materials Science and Engineering, University of Wisconsin-Madison, Madison, WI, 53706, USA
[i] Department of Engineering Physics, University of Wisconsin-Madison, Madison, WI, 53706, USA
[j] Grainger Institute for Engineering, University of Wisconsin-Madison, Madison, WI, 53706, USA

ARTICLE INFO

Keywords:
Microfabrication
Retina
Scaffolds
Stem cells
Tissue engineering

ABSTRACT

Age-related macular degeneration (AMD) causes blindness due to loss of retinal pigment epithelium (RPE) and photoreceptors (PRs), which comprise the two outermost layers of the retina. Given the small size of the macula and the importance of direct contact between RPE and PRs, the use of scaffolds for targeted reconstruction of the outer retina in later stage AMD and other macular dystrophies is particularly attractive. We developed microfabricated, honeycomb-patterned, biodegradable poly(glycerol sebacate) (PGS) scaffolds to deliver organized, adjacent layers of RPE and PRs to the subretinal space. Furthermore, an optimized process was developed to photocure PGS, shortening scaffold production time from days to minutes. The resulting scaffolds robustly supported the seeding of human pluripotent stem cell-derived RPE and PRs, either separately or as a dual cell-layered construct. These advanced, economical, and versatile scaffolds can accelerate retinal cell transplantation efforts and benefit patients with AMD and other retinal degenerative diseases.

1. Introduction

The retina is a thin, multi-layered sensory tissue lining the back of the eye that is capable of detecting light through the stimulation of cone and rod photoreceptors (PRs). PRs are specialized neurons located deep within the retina that capture photons and initiate biochemical and electrical signals that sequentially travel through the inner retinal circuitry to the optic nerve and visual cortex. The homeostasis and functionality of PRs depend largely on retinal pigment epithelial (RPE) cells [1,2], which form a monolayer that separates PRs from the vascular choroid. RPE cells interact with PRs and perform numerous critical functions that support PR health and activity (e.g., nutrient delivery, waste product removal, ion and fluid regulation, retinoid recycling, etc.) [1,2]. The RPE monolayer also forms the outer blood-retinal barrier, which prevents choroidal neovascularization in age-related macular degeneration (AMD) and other macular diseases and helps promote a relatively immune-privileged environment [3]. Thus, direct contact between the multicellular PR layer and the RPE monolayer is important for optimal visual function [1,2].

The most important region of the retina in humans and nonhuman

Peer review under responsibility of KeAi Communications Co., Ltd.
* Corresponding author. Department of Ophthalmology and Visual Sciences, University of Wisconsin-Madison, Madison, WI, 53705, USA.
** Corresponding author. Department of Ophthalmology and Visual Sciences, University of Wisconsin-Madison, Madison, WI, 53705, USA.
*** Corresponding author. Department of Electrical and Computer Engineering, University of Wisconsin-Madison, Madison, WI, 53706, USA.
E-mail addresses: dgamm@wisc.edu (D.M. Gamm), shaoqingong@wisc.edu (S. Gong), mazq@engr.wisc.edu (Z. Ma).
[1] These authors contributed equally to this work.

https://doi.org/10.1016/j.bioactmat.2023.07.019
Received 9 March 2023; Received in revised form 27 June 2023; Accepted 22 July 2023

primates is the macula, a small (5 mm in diameter) centrally located area responsible for high acuity and color vision required for reading, face recognition, and driving a car, among many other tasks. The most prevalent blinding disorder of the outer retina is AMD, which causes primary dysfunction and death of macular RPE followed by central blindness due to secondary loss of the overlying PRs [4]. AMD currently affects more than 11 million people in the United States, a number that is expected to double by 2050 [5]. Not unexpectedly, AMD imposes a significant economic burden in the United States, estimated in 2017 at $134.2 billion [6]. Worldwide, 288 million people will be living with AMD by 2040 [7].

AMD manifests in two broadly defined forms: (1) "dry" AMD, characterized by sub-RPE drusen deposits and slow, inexorable vision loss due to death of RPE and PR cells, and (2) "wet" or neovascular AMD, characterized by aberrant proliferation and leakage of choroidal vessels in the subretinal space, which causes rapid vision loss and RPE and PR atrophy [8,9]. In both forms of AMD [9], as well as in certain retinal injuries (laser ocular injury) [10–12] and inherited macular dystrophies (e.g., Stargardt disease and Best disease) [13,14], loss of both RPE and PRs is the final and irreversible consequence. Intravitreal injection of anti-angiogenic biologics has become a mainstay for the treatment of wet AMD [15,16]; however, such therapies are not always effective, require repeated injections, and cannot restore dead cells. Therapeutics aimed at quelling complement activation in dry AMD have also shown promise, albeit again only at earlier stages of disease prior to cell loss [17–19]. Optogenetic therapies bypass RPE and PRs and thus are a consideration at later disease stages, but they have multiple challenges and bypass normal retinal processing, limiting their potential for macular disorders [20]. In contrast, cell replacement approaches theoretically could reconstruct native circuitry, provided the donor cells display sufficient structural and functional authenticity and can be delivered to the subretinal space in a safe, targeted manner that recapitulates the layered architecture of the outer retina. To address these significant yet surmountable challenges, the National Eye Institute created the Audacious Goals Initiative, which has led to multiple important advancements [21].

Recently, human pluripotent stem cell (hPSC)-derived PRs – and cones in particular – were shown to possess numerous intrinsic properties essential for cell replacement therapies [22,23]. These properties include the ability to (1) respond to wavelength-specific light on par with Macaque foveal cones [24]; (2) support metabolic demands via generation of NADPH [25]; (3) extend axons [26]; and (4) undergo de novo synaptogenesis [27] after removal from an organoid environment. Combined with extensive evidence demonstrating the authenticity of hPSC-RPE [28–30], the cellular building blocks for dual RPE:PR reconstruction in AMD and other macular disorders are now available. Still lacking, however, is a reproducible, economic, and commercially feasible means of precisely packaging these two cell layers for delivery to the human macula [22,23].

The simplest strategy for RPE and/or PR replacement is to inject cell suspensions directly into the subretinal space [31,32]. However, there are limitations to this approach, particularly for the treatment of macular diseases, which relies upon endogenous re-establishment of the RPE and PR layers within a very small target area. In addition, injection of mixed cell suspensions often results in a disorganized cell mass in the subretinal space and may lead to donor cell damage from shear stress and reflux into the vitreous cavity with unintended adverse effects after transplantation [33,34]. Biocompatible and biodegradable cell-seeded scaffolds overcome these issues by allowing precise placement of pre-formed cell layers in focal areas of cell loss [35].

In the past decade, engineering advances have produced planar RPE scaffolds capable of delivering fully differentiated hPSC-RPE monolayers as a regenerative strategy for early-stage AMD [36–40]. More recently, our research team has generated biocompatible and biodegradable PR scaffolds with arrays of 3D microstructures ("wine glass" [41] and "ice cube tray" [42] designs) using a thermo-curable poly (glycerol sebacate) (PGS) polymer and succeeded in creating scaffolds that support the formation of a layer of hPSC-PRs alone [41,42]. These PGS microscaffolds degraded steadily *in vivo* within the subretinal space of rats [42], similar to results achieved with other PGS-based scaffolds [43,44]. However, there is currently no single scaffold that supports production of a stable, ordered RPE:PR bilayer for the treatment of AMD or other macular disorders caused by the death of both cell types [45]. Here, we describe the production, photocuring, and cell seeding of a microfabricated, "honeycomb" (HC) outer retinal scaffold array (referred hereon as a "microscaffold") that achieves this important goal in a consistent, efficient, and economical fashion. Our novel HC pattern design offers advantages over previously described micromolded scaffolds, including 3D wells optimized for dual seeding of RPE and PR cell layers at high densities that maintain mechanical characteristics (e.g., modulus) and dimensions suitable for surgical delivery to the subretinal space. The elastomeric stamp material (i.e., polydimethylsiloxane, PDMS) is engineered and optimized to fine-tune its elasticity and rigidity, and the biodegradable PGS scaffolding material and subsequent curing process were altered to drastically speed up the manufacture of HC scaffolds from days (via thermo-curing) to minutes (via photocuring), which also substantially reduces production costs while remaining clinical good manufacturing process (GMP)-compliant.

2. Materials and methods

2.1. Materials

Information regarding the chemicals used in this work can be found in the Supporting Information.

2.2. Fabrication of the Si master mold

On a clean Si wafer, an array of hexagonal circle patterns for the fluid channels was defined using a photolithography (AZ2020) process and etched with a DRIE process. During the DRIE process, etch/passivation cycles, etch/passivation time per cycle, plasma power, Inductively Coupled Plasma (ICP) power, and $SF_6/O_2/C_4F_8$ gas flows were 93/93 cycles, 10/5 s, 11.7 W, 600 W, and 102/12/100 sccm, respectively. The diameter and depth of the etched fluid channels were 4.1 μm and 28.2 μm, respectively (Fig. S5). After removing the photoresist on the Si wafer with organic solvents (i.e., acetone and isopropyl alcohol) and piranha solution, hexagonal grid patterns for the cell capture wells were formed via a photolithography (AZ2070) process. During the photolithography, the processing time of UV exposure was 48 s and the processing time and temperature of the post-exposure bake were 3 min and 120 °C, respectively. After the development process of photoresist using a chemical developer (AZ 917) for 12 min (1 min 30 s × 8 times, separately), a subsequent hard-bake (130 °C, 2 min) was carried out to toughen the photoresist, so that it could withstand the plasma etching during the DRIE process without any loss of materials. Then, a CF_4 plasma treatment (CF_4 gas, 40 mTorr, 250 W, 40 s) followed by oxygen plasma treatment (O_2 gas, 120 mTorr, 100 W, 1 min) was conducted to remove any remaining organic contaminants on the surface of the Si wafer. Thereafter, the cell capture wells were created by the same procedure that was utilized for generating the fluid channels, with the exception of different etch/passivation cycles for the DRIE process (104/104 cycles). After the DRIE process, the Si master was cleaned with organic solvents and piranha solution and treated with oxygen plasma for 20 s at a plasma power of 40 W, pressure of 120 mTorr, and O_2 gas flow rate of 20 sccm to remove any remaining organic contamination. Finally, the fabricated Si master was coated with a Teflon-like polymer film, which served as a chemically inert passivation layer, using a DRIE process (C_4F_8 = 97 sccm, time = 1 min) to make the surface of the Si master hydrophobic.

2.3. Fabrication of the Hybrid-PDMS stamp

The soft-PDMS precursor was first prepared by mixing and degassing 22.4 g of silicone elastomer base and 5.6 g of curing agent (Dow Sylgard 184 silicone elastomer kit). Thereafter, the hard-PDMS precursor was fabricated by mixing 6.8 g of vinyl PDMS prepolymer (VDT-731), 36 μL of a Pt catalyst (SIP6831.2LC), 100 μL of 2,4,6,8-Tetramethyl-2,4,6,8-tetravinylcyclotetra-siloxane, and 2 g of a hydrosilane pre-polymer (HMS-301). Next, 7 g of the hard-PDMS precursor was poured into the soft-PDMS precursor, mixed for 7 min, and degassed in a vacuum desiccator for 10 min to remove bubbles from inside the hybrid-PDMS mixture. The mixture was then poured onto the resulting Si master and cured at room temperature for 12 h, followed by an extra curing session in an oven at 60 °C for 2 h. After curing, the hybrid-PDMS stamp (2 cm × 2 cm × 0.6 cm size) was peeled off from the Si master using a metal tweezer and cut with a razor blade to obtain four sets of 1 cm × 1 cm x 0.6 cm cubes. The stamps were then cleaned by gently spraying isopropanol onto their surface and carefully blow-drying with nitrogen. In order to facilitate a hydrophobic silane coating (anti-stick coating) during the next step, the stamps were pretreated with oxygen plasma using RIE (plasma power: 40 W, working pressure: 120 mTorr, flow rate: 30 sccm, and processing time: 20 s). Thereafter, the opposite side of the stamps' micro-patterned surface was attached to a glass slide to protect the opposite surface from being covered by the silane coating, thus allowing an efficient UV curing process of PGS through the stamps. Lastly, the entire apparatus (i.e. four stamps on a glass slide) was placed in a desiccator with 400 μL of trichlorosilane (SIT8174.0) and degassed for 12 h at room temperature to allow the stamps' surface to be fully covered with evaporated silane.

2.4. Synthesis of PGS prepolymer

Equimolar glycerol (9.20 g, 100 mmol) and sebacic acid (20.2 g, 100 mmol) were added in a 100-mL Schlenk flask and mixed at 120 °C under nitrogen for 24 h. Thereafter, the pressure was reduced to 0.1 atm for 0.5 h to evaporate all moisture, and further reduced to 1 mbar using the vacuum pump for 18 h at 120 °C to promote polycondensation. The PGS prepolymer was a white wax-like solid after cooling to 20 °C. The cooled PGS prepolymer was then used for thermo-curing process and subsequent reactions without any purification.

2.5. Synthesis of photocurable PGS prepolymer

PGS prepolymer (5.0 g, 19.4 mmol repeating units) was dissolved in anhydrous DCM (50 ml) containing 4-methoxyphenol (1,000 ppm, 5.0 mg) and triethylamine (2.70 mL, 19.4 mmol). Methacrylic anhydride (1.44 mL, 9.7 mmol) was added dropwise (1–2 droplets/s) into the PGS prepolymer solution while stirring in an ice bath for 1 h. The reaction was then continued at 20 °C in the dark for 24 h, followed by further addition of 4-methoxyphenol (1,000 ppm, 5.0 mg) to the reaction solution. The reaction mixture was then repeatedly precipitated in diethyl ether (250 mL) and redissolved in DCM (50 mL) for three cycles. Thereafter, the crude product solution in DCM was washed with saturated brine (pH 3–4, adjusted with 1 M HCl) three times and dried with anhydrous $MgSO_4$ overnight in the presence of 4-methoxyphenol (500 ppm, 2.5 mg). After removal of $MgSO_4$ and solvents, the photocurable PGS was collected and stored at −20 °C. The chemical structure of the photocurable PGS prepolymer was characterized by 1H NMR (400 MHz, solvent: $CDCl_3$).

2.6. Fabrication of photocurable PGS microscaffold

A tube containing photocurable PGS prepolymer blended with GMA (10 wt%) and DMPA (1 wt%) was placed in a vacuum oven (60 °C and <1 mbar) for 20 min in order to melt the photocurable PGS mixture. Approximately 10 mg of the mixture was put on a micro-patterned surface of four hybrid-PDMS stamps via a syringe and degassed in the vacuum oven at 60 °C for 30 min to remove bubbles inside the photocurable material. Thereafter, the stamp was flipped over onto a clean Si wafer. This apparatus (i.e., Si wafer, photocurable material, and stamps) was subsequently placed into the vacuum oven and degassed under a high vacuum (<1 mbar) at 60 °C for 1 h to remove bubbles between the stamps and the Si wafer. During this degassing process, the vacuum oven was vented with nitrogen gas every 10 min to facilitate the removal of bubbles. A 5 × 5 inch quartz plate followed by weights totaling 3120 g (Fig. S12) were then placed on the stamps at room temperature with the stamps' surface (i.e., the opposite side of the stamps' micro-patterned surface) left uncovered by the weights to enable UV curing of PGS through the stamps. The whole apparatus was placed back into the oven at 60 °C for 10 min to liquefy the photocurable material so that the fluid channels would be uniformly opened by the pressure of the overlying weights. Next, the apparatus was placed into a UV curing chamber and cured by UV light (wavelength at 365 nm, 10 mW/cm^2) in a nitrogen atmosphere at room temperature for 30 min to allow complete photocuring. After curing, the apparatus was left at room temperature for 12 h to completely dry any remaining solvents in the photocured PGS that were not fully evaporated during the degassing and curing process. The stamps were then cut horizontally using a razor blade to ~1 mm thickness so that, in the next fabrication step, the PGS scaffolds could be easily delaminated from the stamps by a sonication process in isopropanol (which causes polymer swelling). The apparatus was then immersed in isopropanol and sonication-treated for 4 h. For the first 2 h, both the PGS scaffolds and the stamps were detached together from the Si wafer, while during the last 2 h the PGS scaffolds were delaminated from the stamps. The delaminated PGS scaffolds were transferred onto a Teflon plate using a transfer pipet, and a few drops of DI water were applied to the surface of the scaffolds to allow the swollen scaffolds to return to their original shape. Finally, the PGS scaffolds were carefully blow-dried with nitrogen gas (Fig. S13a).

2.7. Mounting microscaffolds on transwell inserts

First, the thin porous polyester membrane of a transwell insert was removed using a biopsy punch with a diameter of 5 mm. Liquid soft-PDMS was then prepared by mixing the Dow Sylgard 184 silicone elastomer base and curing agent (4:1) and applied to the transwell insert along the edge of the punched hole to serve as an adhesive (Fig. S13b). Next, the transwell insert was aligned and placed onto the microscaffold prepared on a Teflon plate (Fig. S13c) and cured in an oven at 60 °C for 4 h (Fig. S13d). After curing, isopropanol was sprayed on the microscaffold to promote swelling (Fig. S13e) and both the transwell insert and microscaffold were carefully detached from the Teflon plate. The transwell insert was snapped into a transwell holder for cell culture use (Fig. S13f). Fig. S13g shows six microscaffolds mounted onto *in vitro* transwells. In order to activate/functionalize the scaffold surface and promote thorough laminin coating and uniform cell capture, brief oxygen plasma treatment (O_2 gas, 20 sccm, 120 mTorr, 40 W, 40 s) was conducted on the top and bottom surfaces of the microscaffold.

2.8. Tensile test

The hybrid-PDMS films (~1.8 mm in thickness) were prepared using various mixing ratios of the hard-PDMS and soft-PDMS precursors under the optimal curing conditions (25 °C for 12 h followed by 60 °C for 2 h). The hybrid-PDMS films were cut with a dumbbell-shaped (ASTM D638 Type V) die, with three replicates for each sample. Tensile tests were carried out using a pre-tension of 0.1 N and an extension rate of 10 mm min^{-1} (Instron, 5848, with a 50 N load cell). The stress-strain curves were recorded and Young's moduli were calculated.

2.9. hPSC culture and retinal differentiation

Retinal organoids were generated using a well-established protocol for retinal differentiation [25,46]. Briefly, WA09-CRX$^{+/tdTomato}$ hPSCs were maintained in mTeSR plus media on Matrigel-coated 6-well plates (Thermo Fisher Scientific). Free-floating embryoid bodies (EBs) were generated by lifting hPSCs with ReLeSR (0.7ml/well) (STEMCELL Technologies) and gradually exposed to Neural Induction Media (NIM) [1:1 (DMEM):F12 (Thermo Fisher Scientific), 1x MEM-nonessential amino acids (NEAA) (Thermo Fisher Scientific), 1 × GlutaMAX (Thermo Fisher Scientific), Heparin (2 mg/ml; Sigma-Aldrich), and 1% N2 supplement (Thermo Fisher Scientific)] over 4 days followed by a pulse of BMP4 (0.75 nM, R&D Systems) in NIM media at day 6. EBs were then plated at day 7 on Matrigel-coated 6-well plates at a density of approximately 150–200 EBs per well. Thereafter, half of the media was replaced with fresh NIM media, and on day 16 the media was replaced by Retinal Differentiation Medium [RDM; DMEM:F12 3:1, 1x MEM NEAA, 1x antibiotic/antimycotic (Thermo Fisher Scientific), 1x GlutaMAX, and 2% B27 supplement (Thermo Fisher Scientific)]. Between days 25–30, 3D retinal organoid structures were manually dissected using an MSP ophthalmic surgical knife (Surgical Specialties Corporation). Retinal organoids were cultured long-term in poly-HEMA-coated flasks (polyHEMA, Sigma) and fed twice weekly with 3D-RDM media [DMEM:F12 3:1, 1x MEM NEAA, 1x antibiotic/antimycotic (Thermo Fisher Scientific), 1x GlutaMAX, 2% B27 supplement, 5% FBS, 100 μm taurine, 1:1000 CD lipids (11905031, Thermo Fisher)]. Retinal organoids were monitored for the expression of TdTomato using an epifluorescence microscope until they reached Stage 2 (~D120) to ensure peak PR differentiation.

2.10. Differentiation of hPSCs to RPE

1013.202 iPSCs were reprogrammed from somatic cells by CDI (WI, USA) and maintained in mTeSR plus media on Matrigel-coated 6-well plates. iPSCs were differentiated to RPE as previously described [28–30]. Briefly, free-floating EBs were generated using ReLeSR and weaned into NIM media over the course of 4 days. On day 7, EBs were plated on natural mouse laminin 111 (Thermo Fisher Scientific, Cat# 23017015)-coated 6-well plates. On day 16, optic vesicle colonies were mechanically lifted and discarded, and the remaining attached adherent cells were maintained in RDM without vitamin A (RDM(-RA)) [(DMEM: F12 (3:1), 2% B27 without vitamin A (Thermo Fisher Scientific, Cat# 12587010), 1x antibiotic/antimycotic)]. SU5402 (10 μM, Sigma-Aldrich, Cat# SML0443-25 MG) and CHIR 99021 (3 μM, Tocris, Cat# 4423) were included in the first four RDM(-RA) changes, and on day 70–80 of differentiation, RPE cells were enriched via Magnetic-Activated Cell Sorting (MACS) depletion using human CD24-Biotin (Miltenyi Biotec, 130-098-902) and human CD56-Biotin (Miltenyi Biotec, 130-113-868) as previously reported [39].

2.11. RPE, PR, or Dual RPE + PR seeding on scaffolds

All seeding experiments were performed on 5 mm diameter scaffolds mounted on 6-well transwells that were gas-sterilized and precoated with Laminin 521 (0.05 mg/ml; human recombinant Laminin 521, BioLamina) as previously described [42]. RPE cells were seeded at different densities as indicated in the results section in 400 μl of RDM (-RA) supplemented with 10% FBS and Rho kinase inhibitor (ROCKi; Y-27632). After 2 days, the media was replaced by RDM-RA with 2% FBS and later by RDM(-RA) only. In parallel, RPE cells were seeded on natural mouse laminin-coated 6.5 mm transwells (Corning, #3470) at a density of 5 × 10^4 cells/transwell using the same media as described previously for scaffold seeding. For PR seeding, stage 2 organoids (approximately day 120 of differentiation) were dissociated in 10X TrypLE Select Enzyme (Thermo Fisher Scientific, A1217701) and the dissociated cells were seeded in 400 μl of 3D-RDM media containing ROCKi overnight. For dual RPE + PR seeding, RPE cells were first seeded as described above and incubated for 24 h to facilitate RPE cell adhesion to the scaffolds. Subsequently, dissociated cells suspensions containing PRs were seeded on top of the RPE and incubated for another 7 days. Scaffolds were maintained in 3D-RDM with media changes every two days.

2.12. Immunocytochemistry and microscopy

Scaffolds seeded with RPE, PRs, or dual RPE + PR were fixed in 4% PFA for 30 min at room temperature, washed with 1xPBS, and processed for immunocytochemistry as previously reported [42]. Briefly, scaffolds were incubated in blocking solution [10% normal donkey serum, 5% BSA (MilliporeSigma) and 0.5% Triton X-100 (MilliporeSigma) in 1x PBS)] for 1 h at room temperature followed by incubation overnight at 4 °C with one or more of the following commercially available primary antibodies: Rabbit anti-ZO-1 (Thermo Fisher Scientific; Cat #61–7300, 1:100); Mouse anti-MITF (Exalpha, X1405 M, 1:200); Mouse anti-ZO-1 (ThermoFisher/Invitrogen, Cat #33–9100, 1:100); Goat anti-tdTomato (SICGEN; Cat# AB8181-200, 1:300); or Rabbit anti-Recoverin (Proteintech, 10073-AP, 1:1000). Secondary antibodies (Alexa Fluor 488, Alexa Fluor 545, and Alexa Fluor 633, Thermo Fisher Scientific) were diluted 1:500 in blocking solution and incubated for 1 h at room temperature. Scaffolds were then removed from transwells and mounted in Prolong Gold Antifade containing DAPI for nuclei counterstaining (Thermo Fisher Scientific) before being overlaid with a coverslip. A Nikon ECLIPSE Ti2-E widefield fluorescence microscope, equipped with a Multi-wavelength LED Light Engine, was used to capture fluorescence and bright-field images of the fixed scaffolds at different magnifications. High-resolution images and z-stacks (between 70 and 100 optical sections, 2-0.3 μm) were captured using a Nikon A1 Confocal Microscope System and a Plan Apo VC 20X (NA = 0.75) objective. 3D reconstructions, maximum intensity projections (MIP), and denoised images were processed using imaging software (NIS elements v5.30.03). Deconvolution was performed using the NIS Batch Deconvolution tool (v5.30 b11541). Clusters of PR were analyzed for region of interest (ROI) using ImageJ 1.53a macros with the particle analysis tool. Cells were considered positive if the fluorescence intensity was five times or greater than the background intensity.

3. Results and discussion

3.1. Design of honeycomb microscaffolds

As shown in Fig. 1a and b, HC microscaffolds are composed of two critical layers: (1) large hexagonal prism-shaped wells (white) in the top layer that capture, retain, and protect donor cells during transplantation, and (2) smaller, cylinder-shaped fluid channels (orange) in the bottom layer that support water, waste, nutrient and metabolite transport prior to and during scaffold degradation.

For efficient cell capture and retention, the microscaffolds were designed with consideration of the following parameters: (1) Each HC-shaped well should have enough volume and depth (i.e., ~40 μm) to accommodate a monolayer of RPE cells with an overlying multi-cell layer of PRs. (2) The diameter of each cylindrical fluid channel in the scaffold base should be narrow enough (i.e., ≤5 μm) to prevent cell loss or migration through the channels. (3) The scaffold base (i.e., fluid channel layer) should be thick enough (i.e., ~10 μm) to allow safe and secure manipulation before and during transplantation. (4) The aspect ratio of the cell capture wells (i.e., the well width-to-depth ratio) should enable efficient and defect-free scaffold manufacturing. An inappropriate scaffold well aspect ratio can deleteriously affect the scaffold micromolding processes; for example, the microstructures of a PDMS stamp with a high aspect ratio (i.e., >1) can break while demolding the stamp from a Si master (Fig. S1). Thus, with a depth of 40 μm, each side of the well should be long enough (i.e., >40 μm) to maintain an aspect

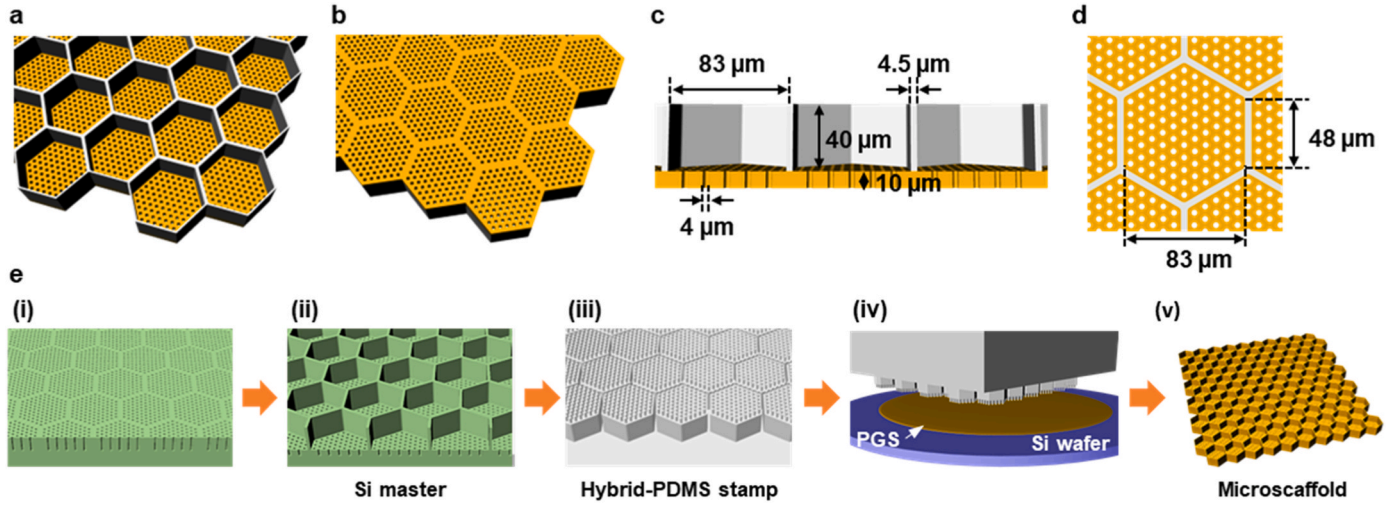

Fig. 1. a-d) Schematic illustration of the honeycomb-shaped microscaffold showing a) a tilted top view, b) a tilted bottom view, c) a cross-sectional view, and d) a top view, respectively. The hexagonal prism-shaped cell capture wells (white in color) are designed to have a large volume (i.e., 40 μm in depth and 48 μm in length for each side of the hexagon) for capturing and retaining both RPE and PR cells in the wells, and the cylinder-shaped fluid channels (orange in color) are tailored to be narrow enough (i.e., ~4 μm) to prevent the seeded cells from migrating through the channels while still supporting cell functions during scaffold degradation. e) Schematic of the procedure for generating a Si master, a hybrid-PDMS stamp, and a photocurable PGS-based microscaffold. (i) Fluid channel- and (ii) cell capture well-etching processes for creating a Si master. (iii) Hybrid-PDMS stamp demolded from the Si master. (iv) The hybrid-PDMS stamp is mounted on liquid PGS on a Si wafer, and after photocuring of the PGS, the stamp is demounted from the scaffold via sonication in 99.97% IPA solution. (v) Completed honeycomb-shaped microscaffold.

ratio less than 1. Detailed information on the dimensions of the HC microscaffold can be found in Fig. 1c and d, and S2.

3.2. Fabrication of Si master molds

Fig. 1e shows the procedure for creating a Si master mold, a PDMS stamp, and a PGS microscaffold. Essentially, the fabrication process for making the HC microscaffolds is similar to the fabrication process that we previously reported for the PR-only, ice cube tray design scaffolds [42] However, changes in the shape and size of the scaffold wells created new challenges within the existing scaffold fabrication workflow. Thus, manufacturing techniques were further optimized by introducing new fabrication processes (e.g., stamp delamination) and re-engineering process parameters (e.g., time and temperature) and molding materials (e.g., hybrid-PDMS and photocurable PGS) to address these challenges.

The HC microscaffold was designed to have deeper wells (~40 μm in depth) than our previous ice cube tray scaffold (~25 μm in depth) [42] to accommodate simultaneous delivery of both RPE and PR cell layers. To produce the Si master mold with the desired dimensions, we increased the processing time of deep reactive ion etching (DRIE). However, this resulted in shallower fluid channels (~3 μm) than desired (~10 μm) (Fig. S3). Previous studies showed that the etching rates of each scaffold layer can vary from the RIE-lag effect due to differences in pattern feature size and from the microloading effect due to pattern density differences [47,48]. We therefore calculated the etch rates for each layer and made deeper fluid channel trenches before etching the cell capture wells. However, photoresist (AZ2070), a light-sensitive material used in photolithography to form a patterned surface coating, remained within the fluid channel trenches during the development process under initial etching conditions (Fig. S4) because the trenches were too deep (28 μm) and narrow (4 μm in diameter). To eliminate photoresist residue within the trenches, the development process time was increased. However, this resulted in over-development of photoresist and subsequent thinning of the well walls, which were easily torn. Therefore, we further optimized the process parameters of photolithography. More specifically, we deliberately over-exposed the photoresist to ultraviolet (UV) light (365 nm) and substantially increased the processing time (from 1 min to 3 min) and temperature (from 110 °C to 120 °C) of the post-exposure bake. With this optimization, we succeeded in increasing the development process time (from 40 s to 480 s) without affecting the width of the well walls, while removing the remaining photoresist residues in the fluid channel trenches (Fig. S5). Finally, a hard-bake (130 °C, 2 min) followed by CF_4 Si etching (20 s) and oxygen plasma treatment (1 min) were performed to ensure complete photoresist removal from the trenches prior to cell capture well-etching.

Fig. 2a shows the scanning electron microscopy (SEM) images of the resulting Si master mold. The Si master mold was free of defects and had clean surfaces in its microstructures. The key feature dimensions of the fabricated Si master were as follows: (1) The diameter and depth of the fluid channels were 4.1 μm and 10.2 μm, respectively. (2) The length for each of the hexagon side and the depth of the cell capture wells were 48.1 μm and 40.1 μm, respectively. (3) The wall width of the cell capture wells and the distance between adjacent fluid channels were both 4.5 μm. To create a PDMS stamp in the next fabrication step, a Teflon-like polymer film with long linear $(CF_2)_n$ chains was coated on the Si master by DRIE-mediated plasma-polymerization of octafluorocyclobutane (C_4F_8) [49], rendering the surface of the Si master chemically inert and hydrophobic. The detailed fabrication processes for generating the Si master are described in the experimental section.

3.3. Fabrication of PDMS stamps

PDMS HC scaffold stamps should not only be mechanically stable for a successful and defect-free micromolding and demolding process in soft lithography, but also able to precisely displace and conform a substrate to assure that all fluid channels are fully open. Thus, two characteristics, stiffness and elasticity, need to be tuned simultaneously to make the required stamp. Toward this end, a previously employed hard-PDMS (SYLGARD® 184) was used as the stamp material [42]. Fig. S6a presents an SEM image of the hard-PDMS stamp demolded from the Si master, which revealed the presence of numerous broken micropillars due to both the brittle nature of the hard-PDMS and the high aspect ratio (~2.49) of the micropillar structures. Since the aspect ratio of the stamp micropillars is crucial to the dual RPE:PR HC scaffold design, we sought to tune the mechanical properties of the stamp materials to facilitate its

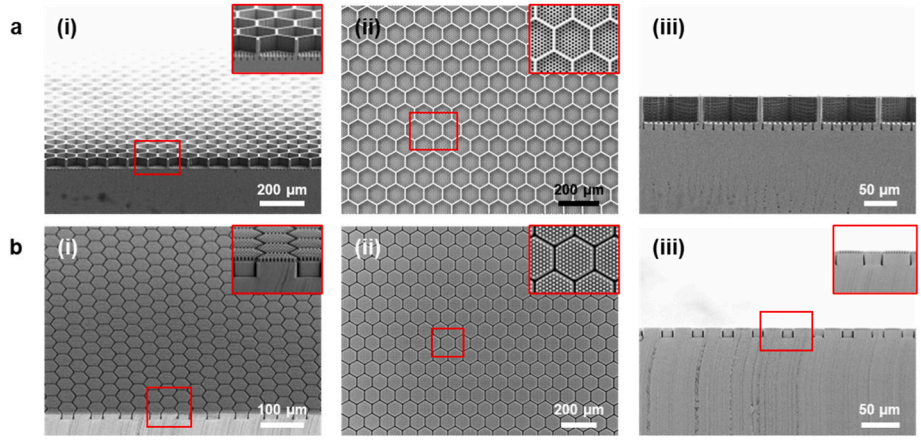

Fig. 2. SEM images of the fabricated a) Si master and b) hybrid-PDMS stamp showing (i) a tilted view, (ii) a top view, and (iii) a cross-sectional view, respectively. The inset images show a magnified view of the microstructures of the fabricated Si master mold and hybrid-PDMS stamp.

successful production. We hypothesized that a hybrid-PDMS could be formed by curing a mixture of hard-PDMS and soft-PDMS, since both types of PDMS form chemical crosslinks using Karstedt's catalyst. Critical parameters, including the mixing ratio of hard-PDMS to soft-PDMS and the curing time and temperature, were optimized to achieve the desired mechanical characteristics of the PDMS stamp (Fig. S6 b-h). Preliminary experiments revealed that hard-PDMS was especially sensitive to heat curing (e.g., hard-PDMS became too brittle when cured at 60 °C for 2 h immediately after mixing). Therefore, hybrid-PDMS was first cured at room temperature, and then cured at higher temperatures in an oven. The empirically determined optimal mixing ratio, curing temperature, and curing time were 1:4 (hard-PDMS:soft-PDMS) and 25 °C for 12 h followed by 60 °C for 2 h, respectively. Further assessment of each stamp material (Fig. S7 and Table S1) showed that 1:4 hybrid-PDMS possessed optimal mechanical properties (Young's modulus: 1.46 MPa and elongation at break: 60.5%) in terms of stiffness and elasticity for the micromolding processes. Fig. 2b shows the SEM images of the successfully fabricated hybrid-PDMS stamp, which was consistently demolded from the Si master without microstructure defects or residues. After demolding, the stamp's surface was treated with oxygen plasma using reactive ion etching (RIE) to facilitate the subsequent hydrophobic and anti-stick silane coating. The detailed process for generating the hybrid-PDMS stamp is described in the experimental section.

3.4. Preparation, optimization, and characterization of photocured PGS

PGS is a biocompatible and biodegradable polyester elastomer with

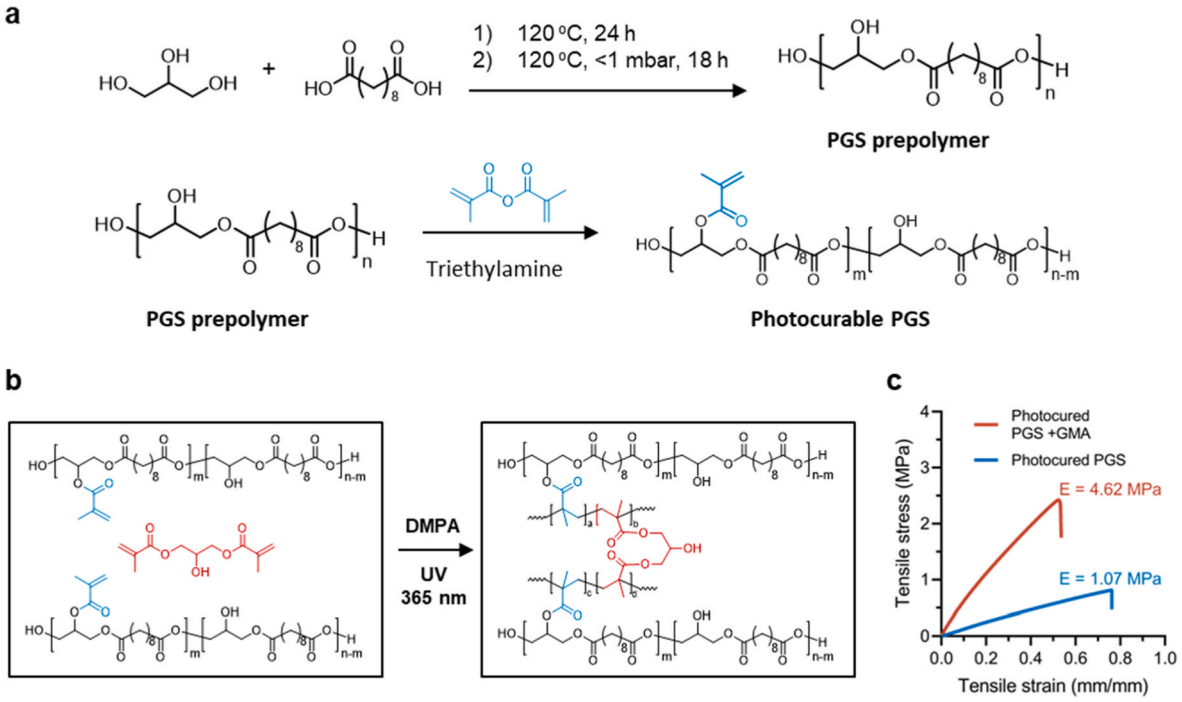

Fig. 3. Synthesis and characterization of the photocurable PGS prepolymer and photocured PGS. a) The synthesis schemes of the photocurable PGS prepolymer. The PGS prepolymer was first synthesized by polycondensation of glycerol and sebacic acid. Thereafter, the photocurable PGS prepolymer was synthesized by esterification between hydroxyl groups on PGS and methacrylic anhydride. b) Under UV at 365 nm and initiated by DMPA, the photocurable PGS prepolymer can be efficiently cured within 5 min, with or without the addition of GMA. c) Stress-strain curves of the photocured PGS with or without 10 wt% GMA. The result indicated that the addition of GMA significantly increased the Young's modulus of the photocured PGS from 1.07 MPa to 4.62 MPa due to its higher crosslinking density.

good manufacturability and sufficient mechanical strength for cell seeding and surgical handling [50–52]. Our previous scaffolds with wine-glass or ice-cube tray well designs were thus fabricated using PGS [41]. However, the previously described PGS prepolymer (i.e., uncured PGS with low molecular weight) requires curing at 120 °C under a high vacuum for 3–4 days to allow complete polycondensation. This thermo-curing process is time-consuming, expensive, and requires a high temperature and a high vacuum, which limit its scale-up manufacturability. We thus hypothesized that conjugation of photocurable groups to the PGS prepolymer would enable ultraviolet (UV) PGS curing and drastically reduce the curing time for the PGS scaffolds from 3-4 days to 30 min [53–55]. As shown in Fig. 3a, methacrylate groups were selected for photocuring PGS via photo-initiated free-radical polymerization. Compared with other photocurable groups, methacrylate groups offer better chemical stability and do not require the addition of thiolate molecules, unlike norbornene groups. The photocurable PGS prepolymer was synthesized by esterification between methacrylic anhydride and hydroxyl groups on the PGS prepolymer, and its chemical structure was verified by 1H NMR, which revealed ~20% methacrylation (Fig. S8) [56].

Under UV light (365 nm, 10 mW/cm^2), the photocurable PGS can be efficiently cured with 2,2-dimethoxy-2-phenylacetophenone (DMPA, the photoinitiator) (Fig. 3b). However, in our preliminary study, the photocured PGS was not as durable as the thermo-cured PGS, leading to defects in the scaffold's microstructures when demounting the stamp from the scaffold (Fig. S9a). Therefore, to enhance the mechanical strength of the photocured PGS, glycerol dimethacrylate (GMA) was blended with the photocurable PGS prepolymer prior to the photocuring process to increase the crosslinking density. GMA was selected because it is unlikely to affect the biocompatibility of the photocured PGS scaffold since the degradation products of GMA (e.g., glycerol) are the same as those of photocurable PGS. The optimal blending ratio of GMA was empirically determined, with 10 wt% showing appropriate mechanical properties as a scaffolding material (Figs. S9b–d). Additional tests demonstrated that the GMA increased the Young's modulus of the photocured PGS from 1.07 MPa to 4.62 MPa and decreased the elongation at break of the photocured PGS from 76% to 52% (Fig. 3c).

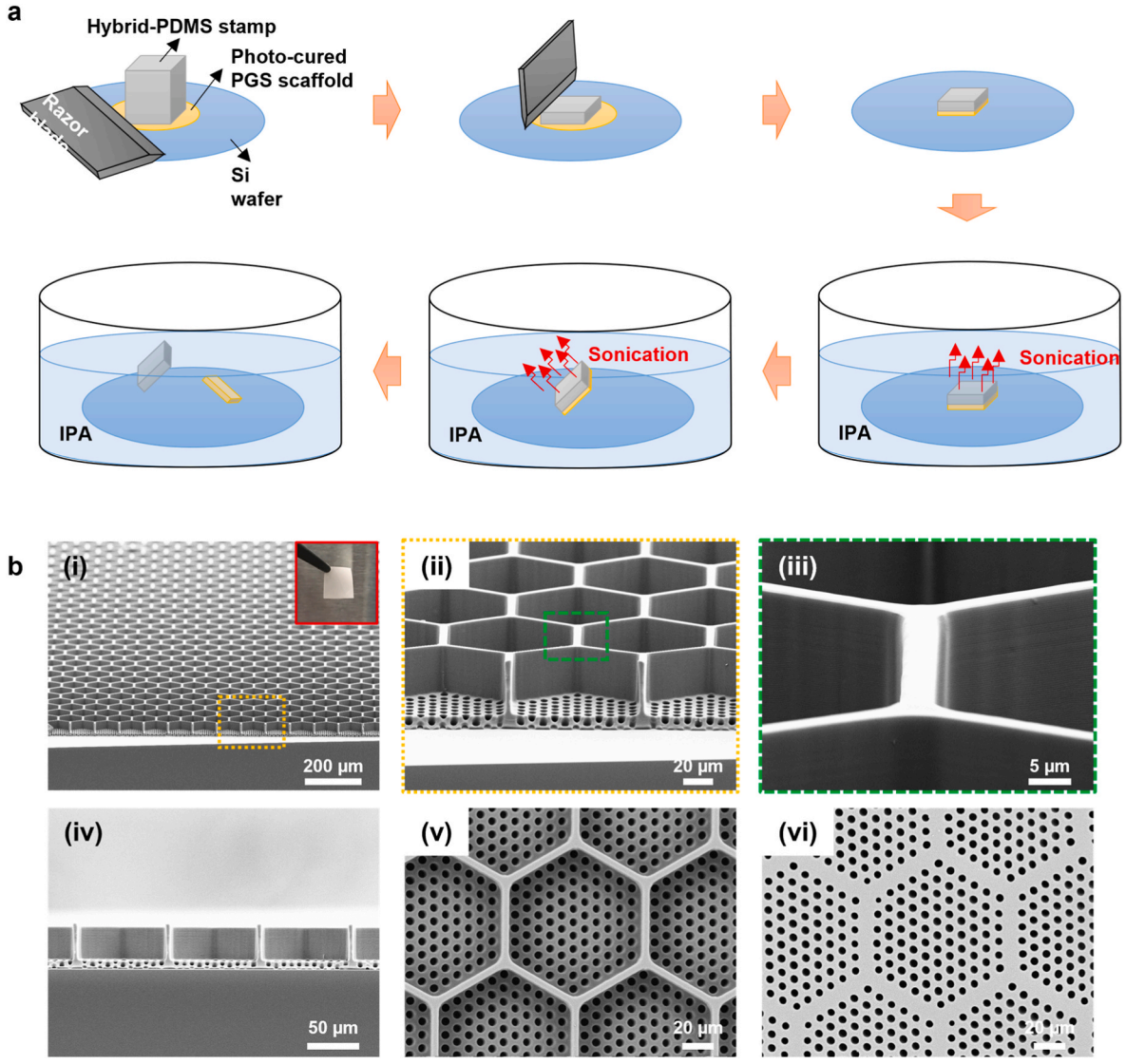

Fig. 4. a) Schematic illustration of the new stamp demounting process. In order to facilitate the scaffold delamination, the stamp was cut horizontally and then vertically using a razor blade, and then sonication-treated in isopropanol (IPA) for 4 h. b) SEM images of the fabricated microscaffold: (i) tilted view (the inset shows a low-magnification photographic image of the fabricated microscaffold held with a tweezer), (ii) magnified view of the scaffold, (iii) magnified view of the wall of a scaffold cell capture well, (iv) cross-sectional view, (v) top view, and (vi) bottom view.

3.5. Fabrication of photocured PGS microscaffolds

Despite optimizing the mechanical properties of the photocurable PGS, some of the HC-shaped wells were torn while manually demounting the stamps from the scaffolds (Fig. S10). This finding was not solely the result of the HC design itself, since PGS scaffolds with ice cube tray-shaped wells having similar dimensions (L/W/H = 50/50/40 μm) were also torn after demounting (Fig. S11). Therefore, a new stamp demounting process was introduced. Fig. 4a describes the final procedure for demounting a hybrid-PDMS stamp from a photocured PGS microscaffold. First, the stamp on the scaffold was cut horizontally to make it thinner so that it could be more easily demounted from the scaffold during sonication in isopropanol. Thereafter, the four sides of both the stamp and the scaffold were vertically cut and removed to let the isopropanol permeate the PGS polymer more quickly, allowing the scaffold to be cleanly detached from the Si wafer. The whole apparatus (i.e., Si wafer, microscaffold, stamp) was then immersed in isopropanol and sonicated for 4 h. Within the first 2 h, the combined microscaffold and stamp were separated from the Si wafer, followed by demounting of the stamp from the microscaffold in the ensuing 2 h. Fig. 4b shows the SEM images of the successfully fabricated HC microscaffold. The HC microstructures were intact over a large area after the HC microscaffold was delaminated from the stamp, with a production yield of over 87%. Of note, this percentage is higher than the ~62% production yield of the ice cube tray design PGS scaffolds that possess similar well dimensions. We also evaluated the long-term *in vitro* stability of the fabricated microscaffolds via optical coherence tomography (OCT) imaging. The microscaffolds showed no significant degradation *in vitro*, with 99.2 ± 3.2% of its baseline thickness remaining after 6 weeks (n = 5) (Fig. S14). A detailed description of the fabrication process for the photocurable PGS microscaffolds can be found in the experimental section.

3.6. Consecutive seeding of hPSC-RPE and hPSC-PR cells in HC PGS microscaffolds

To test the capacity of HC PGS microscaffolds to support a bilayer of RPE and PR cells, the respective optimal cell seeding densities for each cell type were established. First, the optimal density of RPE cells necessary to generate a monolayer across the entire microscaffold was determined. hPSC-RPE cells were generated as previously described [28–30] (also see experimental section) and cultured on human recombinant (hr) laminin 521-coated scaffolds mounted in culture transwells at low (4×10^5 cells/transwell, or ~850 cells/mm^2) or high (7×10^5 cells/transwell, or ~1500 cells/mm^2) density for 7 days. One day after seeding, uniform coverage of the scaffold was observed using the low RPE seeding density (Fig. 5a and b, $n = 9$ microscaffolds), with ample remaining well space for consecutive PR seeding. In contrast, high-density RPE seeding resulted in the formation of RPE clumps that occupied the entire well volume (Fig. S15a, $n = 4$ microscaffolds). Therefore, the low RPE seeding density was selected for more detailed analysis. Low-density RPE-seeded scaffolds were fixed on day 7 and immunostained for ZO-1, a tight junction protein, and microphthalmia-associated transcription factor (MITF), a nuclear marker specific for RPE. Immunostaining results confirmed the viability, identity, and classic morphology of the scaffold-seeded RPE cells relative to parallel cultures of RPE cells seeded directly onto transwells (Fig. 5c and Fig. S15b). High-resolution and 3D confocal image reconstructions showed that the RPE cells grew predominantly as a monolayer that completely and contiguously lined every well of the HC microscaffold (walls and bottom) (Fig. 5d). Importantly, higher magnification 3D reconstructions showed a large remaining space within each HC well 7 days after RPE seeding, sufficient for consecutive seeding of hPSC-PRs (Fig. 5e–g, Supporting video S1). Quantification of RPE cells lining the microscaffolds 7 days post-seeding showed a carrying capacity of 40.4 ± 7.5 RPE cells per HC well ($n = 12$ honeycomb wells, Fig. 5h) or $1.96 \pm 0.36 \times 10^5$ RPE cells per scaffold ($0.997 \pm 1.8 \times 10^4$ RPE cells/mm^2) when they were seeded at the optimized low density of 4×10^5 hPSC-RPE cells per transwell.

While combined replacement of RPE and PRs is required for many macular degenerations, many other retinal diseases result in loss of PRs alone. Thus, we next assessed the potential for hPSC-PRs to be seeded alone on the HC microscaffolds, without prior lining with hPSC-RPE. Human retinal organoids were generated using a previously described protocol [25] (also see experimental section) and human embryonic stem cell reporter line (WA09-CRX$^{+/tdTomato}$) that labels the cytoplasm of all PRs with tdTomato through all stages of differentiation [46]. Retinal organoids were collected and dissociated at ~120 days of differentiation to generate a cellular suspension containing a majority population of tdTomato + PRs as previously reported (Fig. 5i and j) [42,46]. After coating with hrLaminin 521, scaffolds were seeded with 1 million or 3.5 million dissociated cells/transwell (2141 cells/mm^2 or 7494 cell/mm^2, respectively) and cultured for 11 days ($n = 4$ microscaffolds per condition; Fig. S16). Throughout this culture period, uniform PR coverage of HC scaffold wells was observed at both low and high seeding densities with no signs of cellular aggregation (Fig. 5k and l). At day 7, seeded HC microscaffolds were fixed and immunostained to analyze cells expressing tdTomato or recoverin (RCVN), a cytoplasmic marker for PRs (Fig. 5m and n, Supporting video S2). At the 3.5 million cell/transwell seeding density, 3D reconstructions of high-resolution images demonstrated the presence of approximately 85.8 ± 4.9 tdTomato + PR per HC well ($n = 12$ honeycomb wells, Fig. 5h), which extrapolates to $4.16 \pm 0.24 \times 10^5$ tdTomato + PRs within a single microscaffold ($2.1 \pm 0.11 \times 10^4$ PRs cells/mm^2). Importantly, these results reveal that the new HC microscaffolds capture a nearly 5-fold higher density of hPSC-PRs than our previously reported ice cube tray PR microscaffold design (Table S2) [42].

Finally, to test dual RPE:PR seeding efficiency, HC microscaffolds ($n = 10$) were first seeded with hPSC-RPE cells at the previously determined optimized seeding density (4×10^5 RPE cells/transwell), which produced predominantly a monolayer after 24 h in culture (Fig. 6a). One day after RPE seeding, 1 or 3.5 million dissociated retinal organoid cells derived from the WA09-CRX$^{+/tdTomato}$ line were seeded onto the RPE-line HC microscaffold. On the following day (day 2), individual clusters of tdTomato + cells were observed within the majority of the HC wells seeded at 1 million cells/transwell (Fig. 6b and c). Further quantification showed that approximately 79.22 ± 4.53% of all HC wells contained PRs ($n = 8$ microscaffolds). In contrast, HC wells seeded at 3.5 million cells/transwell resulted in the formation of large PR aggregates on the surface of the microscaffolds beginning within 24 h post-seeding ($n = 4$ microscaffolds) (Fig. S17). In contrast to the near immediate surface aggregation observed after high-density hPSC-PR seeding on RPE-lined HC microscaffolds, no surface aggregation occurred at the lower hPSC-PR seeding density after 2 days in culture (Fig. S18, $n = 6$ scaffolds).

To examine the dual RPE:PR seeding of HC microscaffolds in more detail, bilayered constructs were fixed and analyzed by immunocytochemistry 7 days after hPSC-PR seeding. Clusters of RCVN + PRs were retained at the center of the microscaffolds, while MITF + RPE cells formed a monolayer that entirely lined the HC wells (Fig. 6d and e, Supporting video S3). Immunostaining for ZO-1 and RCVN followed by high-resolution 3D image reconstruction showed that hPSC-PRs occupied the center of most HC wells with an underlying, uniform monolayer of RPE cells (Fig. 6f–h, Supporting video S4). We quantified the number of hPSC-RPE cells and hPSC-PRs within the HC microscaffolds and found 42.5 ± 9.2 RPE cells/well ($n = 12$ HC wells, Fig. 6i), or $2.06 \pm 0.44 \times 10^5$ RPE cells per individual microscaffold ($1.05 \pm 0.22 \times 10^4$ RPE cells/mm^2; $n = 4$ microscaffolds). Quantification of hPSC-PRs revealed 53.9 ± 7 hPSC-PR cells/well ($n = 20$ HC wells, Fig. 6i) or $2.61 \pm 0.33 \times 10^5$ hPSC-PRs per individual microscaffold ($1.33 \pm 0.17 \times 10^4$ PRs cells/mm^2; $n = 4$ microscaffolds, Table S3). These results indicate that the photocured, 3D HC microscaffolds can efficiently support robust cultures of hPSC-RPE, hPSC-PRs, or a bilayered combination of hPSC-

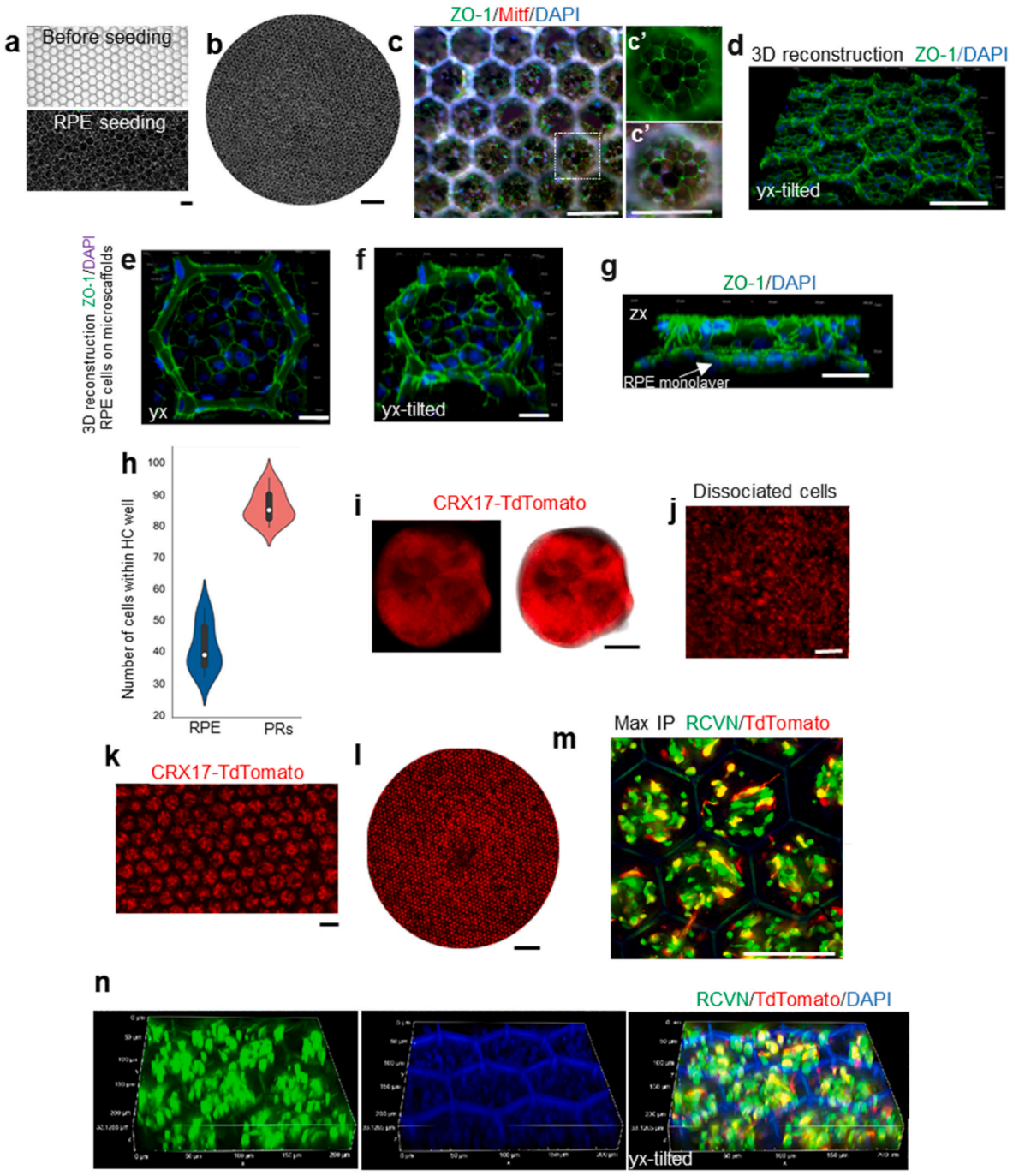

Fig. 5. Microscaffolds seeded with RPE and PRs cells. a) High and b) low magnification brightfield images of microscaffolds before and 24 h after being seeded with hPSCs-derived RPE (RPE) cells. Scale bars: a) 100 μm and b) 500 μm. c) Microscaffolds seeded with RPE cells and analyzed after 7 days by immunocytochemistry staining for ZO-1 (green), MITF (red), and DAPI for nuclei (blue). Scale bars, in c and c' are 100 μm. c') magnified view of the dashed square showed in c showing ZO-1 immunostaining (upper c' panel) and a merged image (lower c' panel). d) Tilted view of a 3D confocal reconstruction showing RPE cells 7 days after seeding on the microscaffold. Scale bar: 100 μm. e-g) Side views of 3D reconstructed images showing the surface of a single honeycomb well covered by a layer of RPE cells 7 days after seeding. Scale bar: 20 μm. h) Violin plots showing the distribution of the number of RPE cells (in blue) or PRs (in red) within individual HC wells 7 days after seeding with 4×10^5 RPE cells/transwell or 3.5×10^6 PRs/transwell. The box plots in the middle of each violin plot delineate the first and third quartiles of the distribution and the central white dot in each box plot indicates the median value. i) WA09-CRX$^{+/tdTomato}$ hPSC-derived retinal organoid after 120 days of differentiation. Scale bar: 500 μm. j) Dissociated cells from CRX17-tdTomato + retinal organoids. Scale bar: 100 μm. k) High and l) low magnifications of live cell fluorescence microscopy images of a microscaffold seeded with PRs from dissociated CRX$^{+/tdTomato}$ organoids two days after seeding. Scale bars: k) 100 μm and l) 500 μm. m) Maximum intensity projection (Max IP) image of a microscaffold seeded with CRX$^{+/tdTomato}$ PRs cells, collected 7 days after seeding and immunostained with recoverin (RCVN, green) and tdTomato (red). Scale bar: 100 μm. n) Tilted view of a 3D confocal reconstruction showing CRX$^{+/tdTomato}$ PRs 7 days after being seeded on a microscaffold. DAPI was used to counterstain the nuclei (blue). Scale in x-axis: 50 μm; in z-axis; 40 μm; in y-axis: 50 μm.

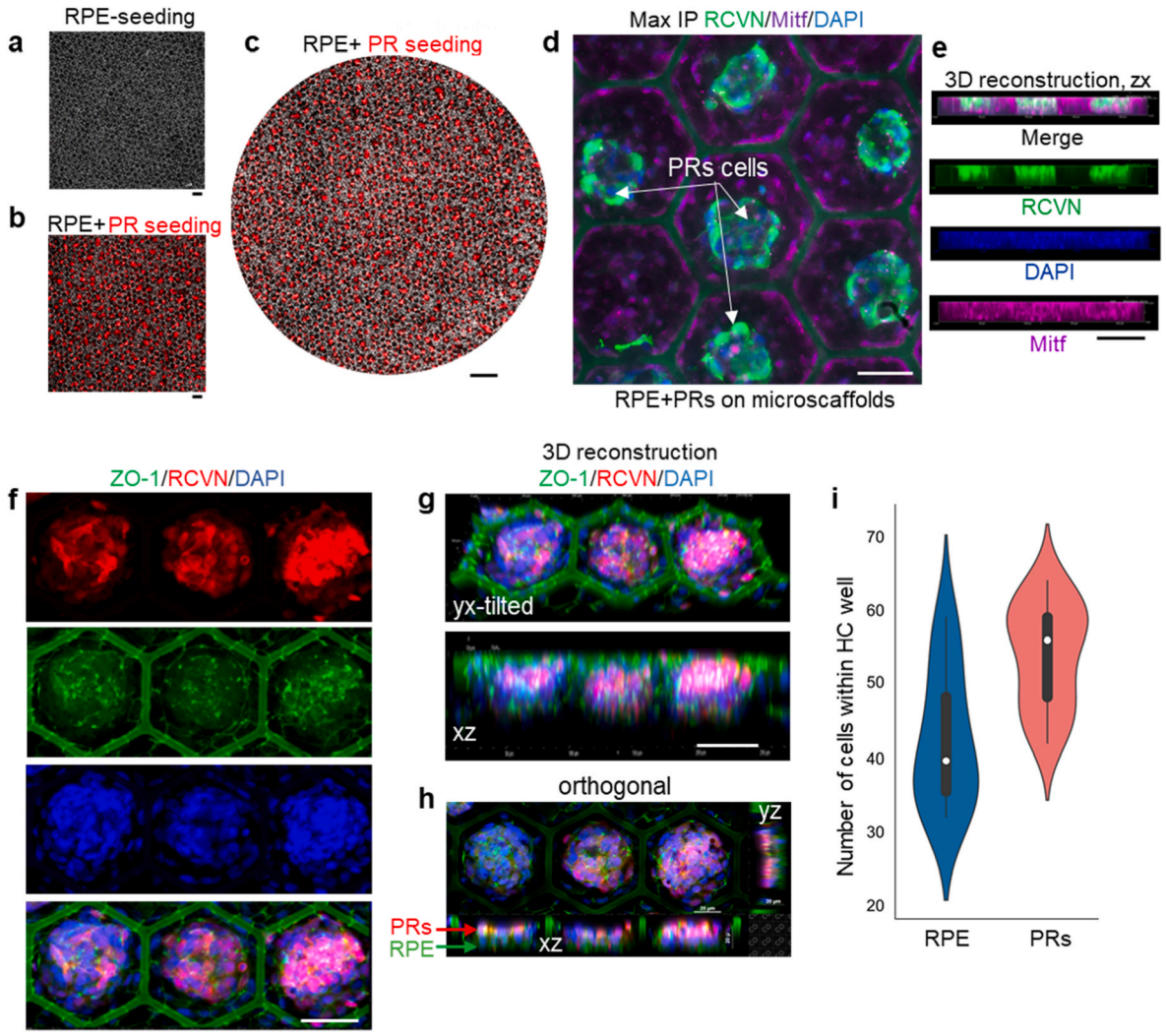

Fig. 6. Seeding of microscaffolds with RPE and PR cells. a) Brightfield images of microscaffolds 24 h after being seeded with 400K RPE cells. b,c) Live cell fluorescence microscopy images of an RPE-coated microscaffold 24 h after seeding with PRs (red fluorescent clusters). Scale bars: a,b) 100 μm and c) 500 μm. d) MaxIP image of microscaffold seeded with both RPE (Mitf + cells) and PRs (RCVN + cells) 7 days after PR seeding. DAPI was used to counterstain the nuclei (blue). Scale bar: 50 μm. e) Side views of 3D reconstructed images from (d). Scale bar: 50 μm. f) High resolution confocal images of PR cells (RCVN + cells) seeded within wells coated with a continuous layer of RPE (ZO-1+ cells). g) Side views of 3D reconstructed images shown in (f). Scale bar: 50 μm. h) Orthogonal projections from the same wells shown in (f) and (g). i) Violin plots showing the distribution of the number of RPE cells (in blue) or PRs (in red) within individual HC wells 7 days after the generation of bilayered RPE:PR cell constructs. The box plots in the middle of each violin plot delineate the first and third quartiles of the distribution and the central withe dot in each box plot indicates the median value.

derived RPE and PRs.

4. Conclusions

We have developed a novel process for the microfabrication and micromolding of 3D PGS outer retinal scaffolds with HC-shaped wells that support (1) production of a predominant monolayer of hPSC-RPE, (2) capture and retention of hPSC-PRs at the highest density thus far described, and (3) consecutive seeding of hPSC-RPE and hPSC-PRs to recreate the outer retina bilayer. To generate the complex 3D HC microstructures within a biocompatible and biodegradable PGS film, new microfabrication techniques and micromolding techniques were developed and processing parameters and molding materials were further optimized. Moreover, it was demonstrated that the photocurable PGS, employed as a scaffolding material, drastically reduced the curing time of PGS from 3-4 days to 30 min. The shape of the HC scaffold microstructures substantially improved the fabrication yield (~87%) compared to PGS ice cube tray scaffold microstructures generated with similar parameters (~62%). Although our previously reported PR-only microscaffolds have the potential to deliver more than 1.74×10^4 hPSC-PRs/mm^2 (but cannot co-deliver RPE and PRs), *in vitro* cell seeding experiments with the HC microscaffold demonstrated the potential to deliver $2.1 \pm 0.11 \times 10^4$ hPSC-PRs/mm^2 alone, or $1.33 \pm 0.17 \times 10^4$ hPSC-PRs/mm^2 after pre-lining the scaffold with a monolayer of $1.05 \pm 0.22 \times 10^4$ hPSC-RPE cells/mm^2. Thus, the shape and dimensions of the HC scaffold microscaffolds succeeded in supporting production of a bilayered RPE:PR construct while maintaining ease of manufacturing and handling. However, the depth of the HC wells (40 μm) remains less than that of the native human photoreceptor layer (~90 μm) [57], leaving room for further design improvements in the future.

The use of scaffolds for the delivery of donor retinal cells to the subretinal space of human subjects has thus far proven to be feasible and safe. Non-biodegradable planar scaffolds capable of delivering hPSC-RPE monolayers were successfully transplanted in animals and human subjects [38,58–60] and, more recently, a clinical trial (NCT04339764 [61]) transplanting autologous iPSC-RPE monolayers was initiated using biodegradable planar scaffolds composed of poly (lactic-co-glycolic acid) (PLGA) [39]. Thus, important surgical and

regulatory considerations related to subretinal scaffold implantation have largely been addressed, although further refinement in the procedure will undoubtedly occur as more experience is obtained in large animal models and humans [62]. We also do not perceive unsurmountable hurdles related to commercial manufacture of the scaffolds described herein. Indeed, the photocured micromolding process used in this study can facilitate the production of a large number of three-dimensional honeycomb scaffolds in a relatively short time frame, which is important for reducing costs and meeting clinical demands. Most importantly, the ability to reproducibly generate a bilayered RPE: PR construct provides a clinically viable platform with which to explore definitive treatment of late-stage macular diseases, including age-related macular degeneration.

Data availability statement

The data that support the findings of this study are available from the corresponding authors upon request.

Ethics approval and consent to participate

Not applicable. The studies were done without experiments or data using animal or human, or animal/human samples.

CRediT authorship contribution statement

In–Kyu Lee: Writing – original draft, co-wrote an initial manuscript draft and contributed equally to this work. performed the experiments. **Ruosen Xie:** Writing – original draft, co-wrote an initial manuscript draft and contributed equally to this work. performed the experiments. **Agustin Luz-Madrigal:** Writing – original draft, co-wrote an initial manuscript draft and contributed equally to this work. performed the experiments. performed the retinal organoid, RPE differentiation and performed the cell seeding experiments. **Seunghwan Min:** Writing – original draft, co-wrote an initial manuscript draft and contributed equally to this work. performed the experiments. **Jingcheng Zhu:** performed the experiments. **Jiahe Jin:** performed the experiments. **Kimberly L. Edwards:** performed RPE culture and differentiation, All authors contributed to data analysis and interpretation including critical discussion and revision of the final manuscript. **M. Joseph Phillips:** Writing – review & editing, conceived and designed the project and reviewed and edited the manuscript. **Allison L. Ludwig:** Writing – review & editing. **David M. Gamm:** Writing – review & editing, Supervision, conceived and designed the project and reviewed and edited the manuscript. supervised this project. **Shaoqin Gong:** Writing – review & editing, Supervision, conceived and designed the project and reviewed and edited the manuscript. supervised this project. **Zhenqiang Ma:** Writing – review & editing, Supervision, conceived and designed the project and reviewed and edited the manuscript. supervised this project.

Declaration of competing interest

D.M.G. is an inventor on patents related to this work filed by the Wisconsin Alumni Research Foundation, Madison, WI (no. 9,752,119, filed 29 April 2016, published 5 September 2017) (no. 9,328,328, filed 24 August 2010, published 3 May 2016). D.M.G., Z.M., M.J.P., and S.G. are inventors on a patent filed by the Wisconsin Alumni Research Foundation, Madison, WI (no. 2017/0226459, filed 5 February 2016, published 10 August 2017). D.M.G., Z.M., M.J.P., S.G., and I.-K.L. are inventors on patents filed by the Wisconsin Alumni Research Foundation, Madison, WI (no. 2020/0010799, filed 9 July 2019, published 01 September 2020) (serial no. 17/769549, filed 10 October 2020, pending). D.M.G. and M.J.P. have an ownership interest in Opsis Therapeutics LLC, which has licensed the technology to generate 3D retinal organoids from pluripotent stem cell sources reported in this publication. The authors declare that they have no other competing interests.

Acknowledgments

This work was supported by the Department of Defense through the Vision Research Program under award no. W81XWH-20-1-0655. Opinions, interpretations, conclusions, and recommendations are those of the authors and are not necessarily endorsed by the Department of Defense. This work was also supported by Fighting Blindness Canada including philanthropic support from Donna Green and Goldie Feldman, Research to Prevent Blindness, RRF Emmett A. Humble Distinguished Directorship, McPherson Eye Research Institute Sandra Lemke Trout Chair in Eye Research (to D.M.G), NIH grant P51OD011106 to the Wisconsin National Primate Research Center, and NIH grant U54HD090256 to the Waisman Intellectual and Developmental Disabilities Research Center. A.L.L. was supported by the UW-Madison School of Veterinary Medicine Dual DVM/PhD Program, NIH/NEI U24 EY029890, and Kirschstein NRSA Predoctoral Fellowship NIH/NEI F30 EY031230. This study was supported in part by a core grant to the Waisman Center from the National Institute of Child Health and Human Development (P50HD105353). Dr. Karla M. Knobel of the CMN Core at Waisman Center.

Appendix A. Supplementary data

Supplementary data to this article can be found online at https://doi.org/10.1016/j.bioactmat.2023.07.019.

References

[1] A. Lakkaraju, A. Umapathy, L.X. Tan, L. Daniele, N.J. Philp, K. Boesze-Battaglia, D. S. Williams, The cell biology of the retinal pigment epithelium, Prog. Retin. Eye Res. (2020), 100846.
[2] O. Strauss, The retinal pigment epithelium in visual function, Physiol. Rev. 85 (3) (2005) 845–881.
[3] A.W. Taylor, Ocular immune privilege and transplantation, Front. Immunol. 7 (2016) 37.
[4] J.B. Hassell, E.L. Lamoureux, J.E. Keeffe, Impact of age related macular degeneration on quality of life, Br. J. Ophthalmol. 90 (5) (2006) 593–596.
[5] D.B. Rein, J.S. Wittenborn, X. Zhang, A.A. Honeycutt, S.B. Lesesne, J. Saaddine, Forecasting age-related macular degeneration through the year 2050: the potential impact of new treatments, Arch. Ophthalmol. 127 (4) (2009) 533–540.
[6] D.B. Rein, J.S. Wittenborn, P. Zhang, F. Sublett, P.A. Lamuda, E.A. Lundeen, J. Saaddine, The economic burden of vision loss and blindness in the United States, Ophthalmology 129 (4) (2022) 369–378.
[7] W.L. Wong, X. Su, X. Li, C.M. Cheung, R. Klein, C.Y. Cheng, T.Y. Wong, Global prevalence of age-related macular degeneration and disease burden projection for 2020 and 2040: a systematic review and meta-analysis, Lancet Global Health 2 (2) (2014) e106–e116.
[8] I. Bhutto, G. Lutty, Understanding age-related macular degeneration (AMD): relationships between the photoreceptor/retinal pigment epithelium/Bruch's membrane/choriocapillaris complex, Mol. Aspect. Med. 33 (4) (2012) 295–317.
[9] C.J. Thomas, R.G. Mirza, M.K. Gill, Age-related macular degeneration, Med. Clin. 105 (3) (2021) 473–491.
[10] R. Narayanan, M. Tyagi, N.K. Sahoo, S. Reddy, A. Pathengay, Accidental self-inflicted handheld laser-induced maculopathy, Ocul. Immunol. Inflamm. (2021) 1–4.
[11] A. Agarwal, A.K. Jindal, G. Anjani, D. Suri, K.B. Freund, V. Gupta, SELF-INFLICTED LASER-INDUCED MACULOPATHY MASQUERADING AS POSTERIOR UVEITIS IN A PATIENT WITH SUSPECTED IgG4-RELATED DISEASE, Retin. Cases Brief Rep. 16 (2) (2022) 226–232.
[12] G.D. Lee, C.R. Baumal, D. Lally, J.D. Pitcher, J. Vander, J.S. Duker, Retinal injury after inadvertent handheld laser exposure, Retina 34 (12) (2014) 2388–2396.
[13] S.H. Tsang, T. Sharma, Stargardt disease, Adv. Exp. Med. Biol. 1085 (2018) 139–151.
[14] S. Singh Grewal, J.J. Smith, A.F. Carr, Bestrophinopathies: perspectives on clinical disease, Bestrophin-1 function and developing therapies, Ther. Adv. Ophthalmol. 13 (2021), 2515841421997191.
[15] F.A. Rezende, E. Lapalme, C.X. Qian, L.E. Smith, J.P. SanGiovanni, P. Sapieha, Omega-3 supplementation combined with anti-vascular endothelial growth factor lowers vitreal levels of vascular endothelial growth factor in wet age-related macular degeneration, Am. J. Ophthalmol. 158 (5) (2014) 1071–1078.
[16] R.M. Galindo-Camacho, C. Blanco-Llamero, R. da Ana, M.A. Fuertes, F.J. Senorans, A.M. Silva, M.L. Garcia, E.B. Souto, Therapeutic approaches for age-related macular degeneration, Int. J. Mol. Sci. 23 (19) (2022).
[17] D.S. Liao, F.V. Grossi, D. El Mehdi, M.R. Gerber, D.M. Brown, J.S. Heier, C. C. Wykoff, L.J. Singerman, P. Abraham, F. Grassmann, P. Nuernberg, B.H.F. Weber, P. Deschatelets, R.Y. Kim, C.Y. Chung, R.M. Ribeiro, M. Hamdani, P.J. Rosenfeld, D.S. Boyer, J.S. Slakter, C.G. Francois, Complement C3 inhibitor pegcetacoplan for

geographic atrophy secondary to age-related macular degeneration: a randomized phase 2 trial, Ophthalmology 127 (2) (2020) 186–195.
[18] S. Hughes, J. Gumas, R. Lee, M. Rumano, N. Berger, A.K. Gautam, G. Sfyroera, A. L. Chan, G. Gnanaguru, K.M. Connor, B.J. Kim, J.L. Dunaief, D. Ricklin, G. Hajishengallis, D. Yancopoulou, E.S. Reis, D.C. Mastellos, J.D. Lambris, Prolonged intraocular residence and retinal tissue distribution of a fourth-generation compstatin-based C3 inhibitor in non-human primates, Clin. Immunol. 214 (2020), 108391.
[19] G.J. Jaffe, K. Westby, K.G. Csaky, J. Mones, J.A. Pearlman, S.S. Patel, B. C. Joondeph, J. Randolph, H. Masonson, K.A. Rezaei, C5 inhibitor avacincaptad pegol for geographic atrophy due to age-related macular degeneration: a randomized pivotal phase 2/3 trial, Ophthalmology 128 (4) (2021) 576–586.
[20] M. Lindner, M.J. Gilhooley, S. Hughes, M.W. Hankins, Optogenetics for visual restoration: from proof of principle to translational challenges, Prog. Retin. Eye Res. 91 (2022), 101089.
[21] R.J. Salowe, J.M. O'Brien, NEI's audacious goals initiative, Ophthalmology 121 (3) (2014) 615–616.
[22] A.L. Ludwig, D.M. Gamm, Outer retinal cell replacement: putting the pieces together, Transl. Vis. Sci. Technol. 10 (10) (2021) 15.
[23] R.N. Van Gelder, M.F. Chiang, M.A. Dyer, T.N. Greenwell, L.A. Levin, R.O. Wong, C.N. Svendsen, Regenerative and restorative medicine for eye disease, Nat. Med. 28 (6) (2022) 1149–1156.
[24] A. Saha, E. Capowski, M.A. Fernandez Zepeda, E.C. Nelson, D.M. Gamm, R. Sinha, Cone photoreceptors in human stem cell-derived retinal organoids demonstrate intrinsic light responses that mimic those of primate fovea, Cell Stem Cell 29 (3) (2022) 487–489.
[25] E.E. Capowski, K. Samimi, S.J. Mayerl, M.J. Phillips, I. Pinilla, S.E. Howden, J. Saha, A.D. Jansen, K.L. Edwards, L.D. Jager, K. Barlow, R. Valiauga, Z. Erlichman, A. Hagstrom, D. Sinha, V.M. Sluch, X. Chamling, D.J. Zack, M. C. Skala, D.M. Gamm, Reproducibility and staging of 3D human retinal organoids across multiple pluripotent stem cell lines, Development 146 (1) (2019).
[26] S.K. Rempel, M.J. Welch, A.L. Ludwig, M.J. Phillips, Y. Kancherla, D.J. Zack, D. M. Gamm, T.M. Gomez, Human photoreceptors switch from autonomous axon extension to cell-mediated process pulling during synaptic marker redistribution, Cell Rep. 39 (7) (2022), 110827.
[27] A.L. Ludwig, S.J. Mayerl, Y. Gao, M. Banghart, C. Bacig, M.A. Fernandez Zepeda, X. Zhao, D.M. Gamm, Re-formation of synaptic connectivity in dissociated human stem cell-derived retinal organoid cultures, Proc. Natl. Acad. Sci. U. S. A. 120 (2) (2023), e2213418120.
[28] R. Singh, W. Shen, D. Kuai, J.M. Martin, X. Guo, M.A. Smith, E.T. Perez, M. J. Phillips, J.M. Simonett, K.A. Wallace, A.D. Verhoeven, E.E. Capowski, X. Zhang, Y. Yin, P.J. Halbach, G.A. Fishman, L.S. Wright, B.R. Pattnaik, D.M. Gamm, iPS cell modeling of Best disease: insights into the pathophysiology of an inherited macular degeneration, Hum. Mol. Genet. 22 (3) (2013) 593–607.
[29] R. Singh, M.J. Phillips, D. Kuai, J. Meyer, J.M. Martin, M.A. Smith, E.T. Perez, W. Shen, K.A. Wallace, E.E. Capowski, L.S. Wright, D.M. Gamm, Functional analysis of serially expanded human iPS cell-derived RPE cultures, Invest. Ophthalmol. Vis. Sci. 54 (10) (2013) 6767–6778.
[30] D. Sinha, B. Steyer, P.K. Shahi, K.P. Mueller, R. Valiauga, K.L. Edwards, C. Bacig, S. S. Steltzer, S. Srinivasan, A. Abdeen, E. Cory, V. Periyasamy, A.F. Siahpirani, E. M. Stone, B.A. Tucker, S. Roy, B.R. Pattnaik, K. Saha, D.M. Gamm, Human iPSC modeling reveals mutation-specific responses to gene therapy in a genotypically diverse dominant maculopathy, Am. J. Hum. Genet. 107 (2) (2020) 278–292.
[31] M. Carido, Y. Zhu, K. Postel, B. Benkner, P. Cimalla, M.O. Karl, T. Kurth, F. Paquet-Durand, E. Koch, T.A. Munch, E.M. Tanaka, M. Ader, Characterization of a mouse model with complete RPE loss and its use for RPE cell transplantation, Invest. Ophthalmol. Vis. Sci. 55 (8) (2014) 5431–5444.
[32] B. Diniz, P. Thomas, B. Thomas, R. Ribeiro, Y. Hu, R. Brant, A. Ahuja, D. Zhu, L. Liu, M. Koss, M. Maia, G. Chader, D.R. Hinton, M.S. Humayun, Subretinal implantation of retinal pigment epithelial cells derived from human embryonic stem cells: improved survival when implanted as a monolayer, Invest. Ophthalmol. Vis. Sci. 54 (7) (2013) 5087–5096.
[33] S.J. Gasparini, S. Llonch, O. Borsch, M. Ader, Transplantation of photoreceptors into the degenerative retina: current state and future perspectives, Prog. Retin. Eye Res. 69 (2019) 1–37.
[34] M.S. Singh, S.S. Park, T.A. Albini, M.V. Canto-Soler, H. Klassen, R.E. MacLaren, M. Takahashi, A. Nagiel, S.D. Schwartz, K. Bharti, Retinal stem cell transplantation: balancing safety and potential, Prog. Retin. Eye Res. 75 (2020), 100779.
[35] L.J. Rizzolo, I.O. Nasonkin, R.A. Adelman, Retinal cell transplantation, biomaterials, and in vitro models for developing next-generation therapies of age-related macular degeneration, Stem. Cells Transl. Med. 11 (3) (2022) 269–281.
[36] A.H. Kashani, J.S. Lebkowski, D.R. Hinton, D. Zhu, M.A. Faynus, S. Chen, F. M. Rahhal, R.L. Avery, H. Salehi-Had, C. Chan, N. Palejwala, A. Ingram, W. Dang, C.M. Lin, D. Mitra, J.C. Martinez-Camarillo, J. Bailey, C. Arnold, B.O. Pennington, N. Rao, L.V. Johnson, D.O. Clegg, M.S. Humayun, Survival of an HLA-mismatched, bioengineered RPE implant in dry age-related macular degeneration, Stem Cell Rep. 17 (3) (2022) 448–458.
[37] A.H. Kashani, J.S. Lebkowski, F.M. Rahhal, R.L. Avery, H. Salehi-Had, S. Chen, C. Chan, N. Palejwala, A. Ingram, W. Dang, C.M. Lin, D. Mitra, B.O. Pennington, C. Hinman, M.A. Faynus, J.K. Bailey, S. Mohan, N. Rao, L.V. Johnson, D.O. Clegg, D.R. Hinton, M.S. Humayun, One-Year follow-up in a phase 1/2a clinical trial of an allogeneic RPE cell bioengineered implant for advanced dry age-related macular degeneration, Transl. Vis. Sci. Technol. 10 (10) (2021) 13.
[38] L. da Cruz, K. Fynes, O. Georgiadis, J. Kerby, Y.H. Luo, A. Ahmado, A. Vernon, J. T. Daniels, B. Nommiste, S.M. Hasan, S.B. Gooljar, A.F. Carr, A. Vugler, C. M. Ramsden, M. Bictash, M. Fenster, J. Steer, T. Harbinson, A. Wilbrey, A. Tufail, G. Feng, M. Whitlock, A.G. Robson, G.E. Holder, M.S. Sagoo, P.T. Loudon, P. Whiting, P.J. Coffey, Phase 1 clinical study of an embryonic stem cell-derived retinal pigment epithelium patch in age-related macular degeneration, Nat. Biotechnol. 36 (4) (2018) 328–337.
[39] R. Sharma, V. Khristov, A. Rising, B.S. Jha, R. Dejene, N. Hotaling, Y. Li, J. Stoddard, C. Stankewicz, Q. Wan, C. Zhang, M.M. Campos, K.J. Miyagishima, D. McGaughey, R. Villasmil, M. Mattapallil, B. Stanzel, H. Qian, W. Wong, L. Chase, S. Charles, T. McGill, S. Miller, A. Maminishkis, J. Amaral, K. Bharti, Clinical-grade stem cell-derived retinal pigment epithelium patch rescues retinal degeneration in rodents and pigs, Sci. Transl. Med. 11 (475) (2019).
[40] C.H. Peng, J.H. Chuang, M.L. Wang, Y.Y. Jhan, K.H. Chien, Y.C. Chung, K.H. Hung, C.C. Chang, C.K. Lee, W.L. Tseng, D.K. Hwang, C.H. Hsu, T.C. Lin, S.H. Chiou, S. J. Chen, Laminin modification subretinal bio-scaffold remodels retinal pigment epithelium-driven microenvironment in vitro and in vivo, Oncotarget 7 (40) (2016) 64631–64648.
[41] Y.H. Jung, M.J. Phillips, J. Lee, R. Xie, A.L. Ludwig, G. Chen, Q. Zheng, T.J. Kim, H. Zhang, P. Barney, J. Min, K. Barlow, S. Gong, D.M. Gamm, Z. Ma, 3D microstructured scaffolds to support photoreceptor polarization and maturation, Adv. Mater. 30 (39) (2018), e1803550.
[42] I.K. Lee, A.L. Ludwig, M.J. Phillips, J. Lee, R. Xie, B.S. Sajdak, L.D. Jager, S. Gong, D.M. Gamm, Z. Ma, Ultrathin micromolded 3D scaffolds for high-density photoreceptor layer reconstruction, Sci. Adv. 7 (17) (2021).
[43] S. Redenti, W.L. Neeley, S. Rompani, S. Saigal, J. Yang, H. Klassen, R. Langer, M. J. Young, Engineering retinal progenitor cell and scrollable poly(glycerol-sebacate) composites for expansion and subretinal transplantation, Biomaterials 30 (20) (2009) 3405–3414.
[44] R. Rai, M. Tallawi, A. Grigore, A.R. Boccaccini, Synthesis, properties and biomedical applications of poly(glycerol sebacate) (PGS): a review, Prog. Polym. Sci. 37 (8) (2012) 1051–1078.
[45] K. Ben M'Barek, C. Monville, Cell therapy for retinal dystrophies: from cell suspension formulation to complex retinal tissue bioengineering, Stem Cell. Int. 2019 (2019), 4568979.
[46] M.J. Phillips, P. Jiang, S. Howden, P. Barney, J. Min, N.W. York, L.F. Chu, E. E. Capowski, A. Cash, S. Jain, K. Barlow, T. Tabassum, R. Stewart, B.R. Pattnaik, J. A. Thomson, D.M. Gamm, A novel approach to single cell RNA-sequence analysis facilitates in silico gene reporting of human pluripotent stem cell-derived retinal cell types, Stem Cell. 36 (3) (2018) 313–324.
[47] S. Franssila, J. Kiihamäki, J. Karttunen, Etching through silicon wafer in inductively coupled plasma, Microsyst. Technol. 6 (2000) 141–144.
[48] B. Wu, A. Kumar, S. Pamarthy, High aspect ratio silicon etch: a review, J. Appl. Phys. 108 (5) (2010) 9.
[49] S.F.F. Laermer, L. Sainiemi, K. Kolari, Handbook of Silicon Based MEMS Materials and Technologies, Elsevier, 2020.
[50] Y. Wang, G.A. Ameer, B.J. Sheppard, R. Langer, A tough biodegradable elastomer, Nat. Biotechnol. 20 (6) (2002) 602–606.
[51] X.J. Loh, A. Abdul Karim, C. Owh, Poly(glycerol sebacate) biomaterial: synthesis and biomedical applications, J. Mater. Chem. B 3 (39) (2015) 7641–7652.
[52] L. Vogt, F. Ruther, S. Salehi, A.R. Boccaccini, Poly(Glycerol sebacate) in biomedical applications-A review of the recent literature, Adv Healthc. Mater. 10 (9) (2021), e2002026.
[53] S. Pashneh-Tala, R. Owen, H. Bahmaee, S. Rekstyte, M. Malinauskas, F. Claeyssens, Synthesis, characterization and 3D micro-structuring via 2-photon polymerization of poly(glycerol sebacate)-methacrylate-an elastomeric degradable polymer, Front Phys-Lausanne 6 (2018).
[54] Y.C. Yeh, L.L. Ouyang, C.B. Highley, J.A. Burdick, Norbornene-modified poly (glycerol sebacate) as a photocurable and biodegradable elastomer, Polym Chem-Uk 8 (34) (2017) 5091–5099.
[55] Y.C. Yeh, C.B. Highley, L. Ouyang, J.A. Burdick, 3D printing of photocurable poly (glycerol sebacate) elastomers, Biofabrication 8 (4) (2016), 045004.
[56] R. Xie, Y.C. Chen, Y. Zhao, N. Yodsanit, Y. Wang, N. Yamamoto, D. Yamanouchi, S. Gong, Injectable hydrogel capable of in situ covalent crosslinking for permanent embolization, ACS Appl. Mater. Interfaces 13 (48) (2021) 56988–56999.
[57] Q. Wang, W.B. Wei, Y.X. Wang, Y.N. Yan, J.Y. Yang, W.J. Zhou, S.Y. Chan, L. Xu, J. B. Jonas, Thickness of individual layers at the macula and associated factors: the Beijing Eye Study 2011, BMC Ophthalmol. 20 (1) (2020) 49.
[58] K. Ben M'Barek, W. Habeler, A. Plancheron, M. Jarraya, F. Regent, A. Terray, Y. Yang, L. Chatrousse, S. Domingues, Y. Masson, J.A. Sahel, M. Peschanski, O. Goureau, C. Monville, Human ESC-derived retinal epithelial cell sheets potentiate rescue of photoreceptor cell loss in rats with retinal degeneration, Sci. Transl. Med. 9 (421) (2017).
[59] N.C. Hunt, D. Hallam, V. Chichagova, D.H. Steel, M. Lako, The application of biomaterials to tissue engineering neural retina and retinal pigment epithelium, Adv Healthc. Mater. 7 (23) (2018), e1800226.
[60] A.H. Kashani, J.S. Lebkowski, F.M. Rahhal, R.L. Avery, H. Salehi-Had, W. Dang, C. M. Lin, D. Mitra, D. Zhu, B.B. Thomas, S.T. Hikita, B.O. Pennington, L.V. Johnson, D.O. Clegg, D.R. Hinton, M.S. Humayun, A bioengineered retinal pigment epithelial monolayer for advanced, dry age-related macular degeneration, Sci. Transl. Med. 10 (435) (2018).
[61] clinicaltrials.gov, Autologous Transplantation of Induced Pluripotent Stem Cell-Derived Retinal Pigment Epithelium for Geographic Atrophy Associated with Age-Related Macular Degeneration, 2023. https://beta.clinicaltrials.gov/study/NCT04339764.
[62] R. Sharma, D. Bose, A. Maminishkis, K. Bharti, Retinal pigment epithelium replacement therapy for age-related macular degeneration: are we there yet? Annu. Rev. Pharmacol. Toxicol. 60 (2020) 553–572.